RPE | Radiation Physics & Engineering
A Peer-Reviewed Journal
Published by K.N. Toosi University of Technology
http://rpe.kntu.ac.ir
Research Article

Radiation Physics and Engineering 2027; ?(?):?–?

Mitigation of photoneutron contamination in high-energy LINACs via component reconfiguration and advanced shielding

Mohammad Hossein Jahanimehr, Seyed Mohammad Mahdi Abtahi*

Faculty of Basic Sciences, Physics Department, Imam Khomeini International University, Qazvin, Iran

HIGHLIGHTS

- Increasing Cerrobend thickness from 8 to 10 cm reduced neutron dose by 23%.
- Increasing BPE thickness from 2 to 4 cm reduced neutron dose by 18%.
- Moving the MLC beneath the primary collimator reduced neutron dose by 44%.
- Replacing tungsten with iron in the primary collimator reduced neutron dose by 10%.
- Flattening-filter removal had no significant effect on neutron dose.

ABSTRACT

Photoneutrons are produced when photons with energies greater than 10 MeV interact with high-Z materials in the accelerator head. This study investigated reducing photoneutron dose by modifying linear accelerator component configurations and using shielding materials, including Cerrobend blocks and borated polyethylene (BPE). We used the MCNPX Monte Carlo code to calculate photon and neutron fluence and dose distributions in a phantom. We evaluated different BPE and Cerrobend thicknesses for their dose-attenuation capabilities. We also examined various accelerator component configurations and calculated neutron fluence and equivalent dose using the F5 tally and dose conversion factors (DFs). Cerrobend placed around the tumor significantly reduced photon dose rates but did not substantially reduce neutron dose. Relocating the multi-leaf collimator (MLC) from below the jaws to below the primary collimator (PC) reduced neutron dose by 44%. Replacing the PC material from tungsten to iron produced a further 10% reduction in neutron dose. Using secondary collimator jaws was associated with lower neutron contamination, whereas raising the MLC increased neutron dose. The greatest neutron dose reduction was achieved with 2-4 cm thick BPE. These findings indicate that strategic modifications to accelerator design, combined with appropriate shielding materials, can effectively reduce neutron contamination during high-energy photon radiotherapy.

KEYWORDS

Photoneutron
Cerrobend block
Borated Polyethylene
Linear accelerator

HISTORY

Received:
Revised:
Accepted:
Published:

1 Introduction

Radiotherapy using medical linear accelerators (LINACs) is a widely used cancer treatment. High-energy accelerators offer benefits over low-energy systems, including increased dose delivery at deeper tissue depth and reduced skin surface dose. The machines also minimize scattered radiation exposure to adjacent healthy tissues (Khan and Gibbons, 2014). Depending on the model, these systems can provide photon beams with nominal energies ranging from approximately 6 to 18 MV, as well as electron beams across clinically relevant energies. Common applications include the treatment of deep-seated tumors-such as malignancies of the head and neck, brain, and prostate-using photon beams, and the treatment of superficial or shallow lesions, including cutaneous tumors, using electron beams. In addition, these machines can deliver three-dimensional conformal radiotherapy (3D-CRT) using fixed or multiple treatment fields (Khan and Gibbons, 2014; Ng et al., 2023). The clinical applications of the Elekta SL25 overlap substantially with those of general-purpose medical linear accelerators; however, the model is distinguished primarily by its specific technical characteristics, available beam energies, and treatment-head design (Martinez-Ovalle et al., 2011). For instance, the FWHM of the Elekta SL25 at 18 MV is narrower than that of the Siemens KDS (1.0 vs. 1.5 MeV), indicating superior beam sharpness, which is advantageous for precision radiotherapy. Furthermore,

*Corresponding author: sm.abtahi@sci.ikiu.ac.ir

https://doi.org/

the two accelerators have incident electron energies of 16.1 MeV and 13.5 MeV, respectively, resulting in a higher maximum bremsstrahlung photon energy for the Elekta SL25. Notably, the Elekta model produces approximately 61% less neutron fluence than the 18 MV Varian linac, potentially reducing the risk of secondary cancer induction during treatment (Martinez-Ovalle et al., 2011).

However, dose deposition in ordinary tissues from external sources such as gamma radiation (from radionuclides within the treatment room) and secondary gamma radiation (from inelastic collisions) remains unavoidable (Cheraghian et al., 2021). Neutron production is a more severe issue in high-energy radiotherapy. Neutrons are formed when high-energy photons (> 10 MeV) collide with accelerator components such as collimators and flattening filters (FF) (Rajesh et al., 2020). Because neutrons have 2-20 times the quality factor of photons, they inflict tremendous damage on patients and staff and can cause secondary malignancies.

In addition to photon interactions with accelerator and treatment-room structures, other processes such as giant dipole resonance (GDR), quasi-deuteron effects, and delta resonance lead to photoneutron production (Naseri and Mesbahi, 2010). The type of electron accelerator also influences neutron yield. Among accelerator components, the target and PC are fixed and cannot be removed or shifted, whereas components like the MLC, FF, and wedges can be removed or modified. Numerous studies have investigated the Influence of accelerator components on the photoneutron production process (Naseri and Mesbahi, 2010; Banaee et al., 2021; Becker, 2007; Ma et al., 2008; Mao et al., 1997; Mohammadi et al., 2015; Paredes et al., 2001; Pena et al., 2005; Zanini et al., 2004). For example, Dwolatabadi et al. reported that the percentage of photoneutron production by collimators ranges between 70% and 90% (Dowlatabadi et al., 2020). Although numerous studies have investigated the role of Cerrobend blocks in photon attenuation (Johns et al., 1983; Sahin et al., 2024; Seif et al., 2017; Tellili et al., 2017; Kumar et al., 2018), only two have focused on their effectiveness in neutron attenuation, and their findings were inconsistent. Tossi et al. showed that Cerrobend absorbs photons and attenuates neutron fluence (Toossi et al., 2018), while Khajetash et al. showed it may increase photoneutron generation (Khajetash et al., 2019).

In this study, we thoroughly investigated the neutron attenuation effect of the Cerrobend block, with particular emphasis on resolving inconsistencies reported in prior research. The study then focuses on determining the optimal amount of boron-loaded polyethylene that effectively reduces neutron fluence while remaining economically feasible. Furthermore, because accelerator components pose significant challenges for photoneutron production, this research proposes an optimized design for accelerator structures to minimize photoneutron generation. Collectively, these objectives address existing gaps in the literature and contribute substantially to improving the performance and cost-effectiveness of shielding systems used in particle accelerators.

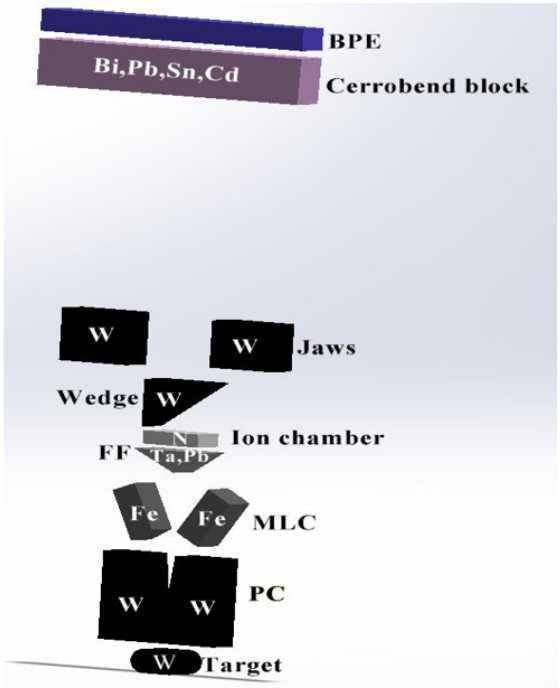


Figure 1: Schematic representation of the symmetric Cerrobend block and its position relative to the various accelerator components, generated from a model designed in SolidWorks.

Table 1: Materials used in the components of the accelerator.

Components of the accelerator	Material
Target	Tungsten (W)
PC	Tungsten (W)
Wedge filter	Tungsten (W)
FF	Lead (Pb) ,Tantalum (Ta)
Ionization chamber	Nitrogen (N)
Secondary collimator jaws	Tungsten (W)
MLC	Iron (Fe)

2 Materials and Methods

2.1 Geometry of linear accelerator

When incident electrons enter a target, they undergo successive interactions and progressively lose kinetic energy until they come to rest within the material. These interactions generate bremsstrahlung photons, whose energy spectrum extends up to the maximum energy of the incident electron beam. The corresponding bremsstrahlung cross sections can be calculated using the formalism proposed by Motz and Koch. Their theory indicates that photon-conversion efficiency depends primarily on the target material's atomic number Z, the incident electron-beam energy, and the target thickness (Koch and Motz, 1959). The Monte Carlo simulation parameters were configured as follows: electron energy of 18 MeV, a beam diameter of 3 mm, and a beam direction aligned with the Z-axis, incident perpendicularly onto the target.

The geometry of the medical linear accelerator (linac) head for the Elekta SL25 model is illustrated in Fig. 1, and the material composition of the simulated head components is summarized in Table 1. The head assembly

Under Proof

comprises the target, primary collimator, FF, ionization chamber, wedge, and jaws.

The target has a cylindrical geometry, with a height of approximately 2 cm and a diameter of about 0.25 cm. The FF, fabricated from a lead-tantalum alloy, is positioned 19 cm from the target. The primary collimator, made of tungsten, is located approximately 1.70 cm below the target and has a height of about 10.80 cm. The physical wedge is approximately 10 cm tall and is positioned 35 cm from the target. The jaws and MLC have heights of approximately 11 and 8 cm, respectively, and are located 45 and 19 cm from the target, respectively. A Cerrobend block with a thickness ranging from 2 to 16 cm was positioned at a distance of 70 cm from the target. In addition, a 2-cm-thick borated polyethylene layer was placed behind the shield, 73 cm from the target. The primary function of the collimator is to direct and confine the photon beam along the desired direction. However, this process inevitably reduces beam intensity because it blocks radiation, which is an inherent technical limitation of collimators.

As the beam propagates further, the photon fluence incident on the FF attenuates. Because the filter is thicker along the central axis and progressively thinner with increasing radial distance from the axis, attenuation is considerably greater at the beam center than in the peripheral regions. The secondary collimators shape symmetric radiation fields, whereas the MLC generates asymmetric fields.

2.2 Angular distribution

High-energy electrons incident on the target produce bremsstrahlung photons. Because the incident electrons have high energy, these photons are emitted predominantly in the direction of electron propagation and within a narrow angular range around the central axis. Consequently, the initial photon angular distribution is strongly forward-peaked, with the photon fluence decreasing as the angle relative to the central axis increases.

Interactions between the X-ray beam and the various components of the accelerator head then modify the beam's spatial and angular distribution. Before interacting with the flattening filter, the photon intensity is higher in the central region than in the peripheral regions. Because the FF is thicker along the central axis and becomes progressively thinner with increasing radial distance from the axis, central-axis photons undergo greater attenuation than those in the peripheral regions. As a result, the photon-intensity distribution across the treatment field becomes more uniform (Khan and Gibbons, 2014).

Photoneutrons produced in high-energy accelerators can generally be classified into two groups. The first group comprises evaporation neutrons, whose energy distribution is approximately Maxwellian. These neutrons are emitted when the energy of the incident photon is distributed among the nucleons of the excited nucleus, allowing a neutron near the nuclear surface to acquire sufficient energy to escape. Owing to the loss of directional information during the formation and subsequent decay of the compound nucleus, evaporation neutrons are characterized by an approximately isotropic angular distribution (Mohammadi et al., 2014b). The second group consists of knock-on neutrons produced through the direct interaction of the incident photon with an individual neutron within the nucleus. In this process, a substantial fraction of the photon energy is transferred directly to the neutron. Consequently, these neutrons generally possess higher energies than evaporation neutrons and exhibit an anisotropic angular distribution, with preferential emission in the forward direction, that is, along or near the direction of the incident photon. Despite their higher energies, knock-on neutrons constitute only a minor fraction of the total photoneutron yield (Facure et al., 2005). Evaporation neutrons account for the dominant component of photoneutron production.

2.3 The metallic alloy Lipotiz (Cerrobend block)

Several systems have been developed to shape the radiation field in radiotherapy, the most well-known being the system described by Powers et al. (Khan and Gibbons, 2014). This system employs a Bend alloy, or Cerrobend, which is a material with a density of approximately 9.4 $g.cm^{-3}$ and a melting point around 70 °C. Cerrobend is an alloy composed of about 50% bismuth (Bi), 26.7% lead (Pb), 13.3% tin (Sn), and 10% cadmium (Cd). Other Cerrobend alloys, such as Tru alloy, Low 147 alloy, Safe alloy, Cast alloy, and Low 136 alloy, differ in density, chemical composition, and physical characteristics (Tellili et al., 2017).

Manufacturing of Cerrobend blocks begins with radiographic simulator films used to define the treatment field and shielding regions. Using a hot wire guided by the film pattern, the technique cuts converging cavities from a block of Styrofoam and then fills them with melted Cerrobend. This technique allows for the precise construction of both positive shielding pieces (e.g., lung blocks) and negative shielding pieces (e.g., head and neck blocks) (Khan and Gibbons, 2014). For the simulation in this study, the shielding block was simplified and modeled as a symmetric cube with dimensions of $50 \times 50 \times 50$ cm^3. Cerrobend is favored in radiotherapy shielding because of its low melting point, high density, and effective photon attenuation, allowing easy molding and customization to protect healthy tissues while minimizing radiation transmission.

2.4 Block Position and Photoneutron Dose Evaluation

A Cerrobend block with a thickness varying from 2 cm to 16 cm, in steps of 2 cm, was positioned 70 cm from the accelerator source upstream. Air measurements of neutron and photon fluence and dose behind the block were made using a point detector (F5 tally) with a radius of 5 cm. Because the F4 tally estimates volume-averaged particle fluence within a defined cell rather than at a single point, it requires specifying a finite scoring volume in the region of interest. In contrast, the F5 tally enables

Uncorrected Proof

particle fluence and dose to be evaluated at an arbitrarily defined point without introducing a physical surface or volume at the detector location. In the present study, photon and neutron fluence and dose were calculated at a detector positioned 5 cm from the central axis. No additional material or geometric structure was introduced into the beam path. Therefore, the F5 point-detector tally was considered the most appropriate scoring method for this analysis. To allow for precise measurement of changes in neutron dose as a function of the thickness of the Cerrobend block, no material was incorporated posterior to the block. The reason was based on design considerations from previous studies that provided inconclusive results on Cerrobend's neutron-shielding properties, even though it is well established as an effective medium for photon-beam attenuation. Thus, a more thorough evaluation of its neutron-attenuation property was warranted. Figure 2 clearly depicts the position of the Cerrobend block relative to the accelerator target.

2.5 Inclusion of BPE

After characterizing the neutron-attenuation capacity of a standalone Cerrobend block, we placed a BPE plate with a thickness ranging from 2 to 10 cm, in 2-cm increments, downstream of the block. Polyethylene is a good medium in slowing down fast neutrons due to the large scattering cross-section of hydrogen despite having a comparably low absorption cross-section in thermal neutrons (Piotrowski, 2020). The addition of boron-at a weight fraction of 4%-improves the neutron shielding ability as a result of the very high thermal neutron absorption cross-section of boron (> 3800 barns) (Wang et al., 2011).

Thermal neutron capture by boron results in secondary emission of gamma radiation, which is still attenuated by the Cerrobend block-the present study aimed to find the optimal BPE thickness that minimizes neutron contamination while being economical.

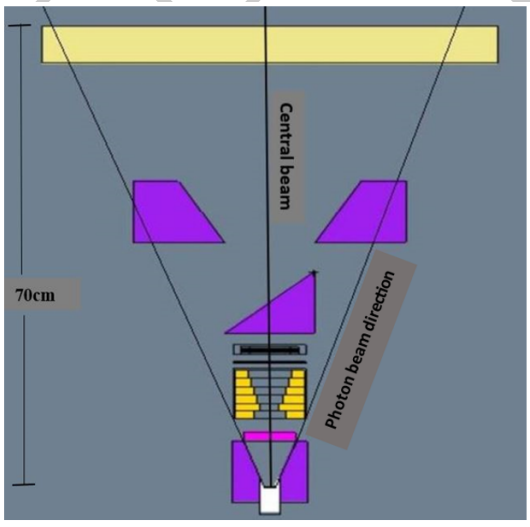


Figure 2: MCNPX Visual Editor rendering of the simulated Elekta SL25 linear accelerator geometry. The arrow indicates the photon-beam propagation direction along the central axis (Z-axis), from the target toward the downstream accelerator components, Cerrobend block, and scoring region.

2.6 Optimization of Accelerator Components

In a bid to reduce neutron contamination even more, a few modifications were made to the accelerator setup. First, the FF was removed, and photon and neutron doses were measured in air. The same was subsequently done for the wedge filter and for the MLC to ascertain eachcomponent's contribution to total dose levels.

To explore the role of component configuration, the MLC was shifted from under the PC to under the jaws (secondary collimator). Besides this, the PC composition was changed from tungsten to iron, based on findings of Naseri et al. (Naseri and Mesbahi, 2010), who proved that the PC was the most important photoneutron generation source. Through these modifications, the accelerator configuration with the minimum neutron dose was determined and documented.

2.7 Verification and simulation

We performed simulations using the Monte Carlo N-Particle eXtended (MCNPX, USA) code version 2.5.0 (Hendricks et al., 2005), developed by Los Alamos National Laboratory, to model particle transport and interactions over a wide energy range. To verify our simulations' accuracy, we based them on Mesbahi et al.'s work (Mesbahi and Nejad, 2008).

Numerical data were obtained from Mesbahi et al.'s graphs with the help of Graph Digitizer software (GetData-Graph-Digitizer.com, Russia). They modeled a medical linear accelerator to calculate photon dose distributions in FF and FF Free modes. They matched the percentage depth dose (PDD) for field sizes 2×2, 5×5, 10×10, and 20×20 cm^2 in a $50 \times 50 \times 50$ cm^3 water phantom at an SSD of 100 cm, and compared their results experimentally. They also plotted the photon spectrum on the water surface using a point detector at a radius of 5 cm and provided a confirmed photon spectrum for this accelerator model. In our study, we also calculated the photon spectrum near the phantom surface at the same 5 cm radius and compared it with their reported spectrum. Using Tecplot 360 EX software (Tecplot, Inc., Bellevue, WA, USA), we calculated an average difference of below 5%, with a lowest spectral difference of 0.3% and an upper limit of 10%.

2.8 Fluence and dose

The DF (Dose Function) card in MCNP was used to calculate equivalent doses from photon and neutron radiation. This card applies energy-dependent fluence-to-dose-equivalent conversion coefficients to particle fluence tallies. First, we calculated photon and neutron point fluences at 2 cm downstream of the Cerrobend block using the F5 point-detector tally. A radial distance of 5 cm from the central axis was assigned to each scoring position. The corresponding DF card, containing the photon and neutron fluence-to-dose-equivalent conversion coefficients, was then applied to each tally. Accordingly, the photon and neutron equivalent doses were calculated at each scoring location. We calculated photon and neutron fluences as

Uncorrected Proof

the number of particles per unit area per incident electron.

We normalized the photon equivalent dose to the absorbed photon dose and reported it in $mSv.Gy^{-1}$. This unit quantifies photon equivalent dose (mSv) per unit absorbed dose (Gy). We calculated neutron equivalent dose relative to photon equivalent dose and expressed it as $mSv.mSv^{-1}$. In other words, the numerator represents the neutron equivalent dose in millisieverts, whereas the denominator represents the photon equivalent dose, also in millisieverts. Although many studies report neutron equivalent dose in $mSv.Gy^{-1}$ (Mendes et al., 2022), the numerical difference is negligible because the radiation weighting factor for photons is unity. Consequently, the numerical value of one gray of absorbed photon dose is approximately equal to one sievert of photon equivalent dose. Therefore, the neutron equivalent dose may be reported in either $mSv.Gy^{-1}$ or $mSv.Sv^{-1}$. However, to maintain consistency between the numerator and denominator and to improve clarity, the present study used the $mSv.mSv^{-1}$ ratio. A value of 1 $mSv.mSv^{-1}$ indicates that one millisievert of neutron equivalent dose is delivered to the tissue for every millisievert of photon equivalent dose.

2.9 Calculation of ambient dose equivalents for photons and neutrons

To estimate the ambient dose equivalent at a distance of 100 cm from the target, an MCNP point-detector tally (F5) was placed on the central beam axis. The F5 tally uses the next-event estimator to estimate the photon and neutron fluences at a specified point by evaluating the probability of particle transport to the detector point, including attenuation along the path.

The ambient dose equivalent, $H^*(10)$ was then calculated using the following relationship (Protection, 2007):

$$H^*(10) = \int_0^\infty \mathrm{d}E\, \phi(E) h^*(E) \tag{1}$$

where $\phi(E)$ denotes the fluence per emitted particle at the point of interest, and $h^*(E)$ represents the corresponding fluence-to-dose conversion coefficient. The conversion-coefficient values were obtained by cubic-spline interpolation of the data reported in the ICRU 57/ICRP Publication 74 tables (Protection, 2007). We calculated the ambient dose equivalent for all accelerator configurations listed in Table 3.

2.10 Annual occupational dose

To estimate the annual dose received by healthcare personnel positioned near the accelerator head, we developed a geometrical model of the medical linear accelerator and the therapist's location using the MCNP code. The scoring point was defined adjacent to the treatment head, 1 m from its external surface. This location was considered representative of the therapist's potential position during patient preparation or transfer.

The model specified the energy spectrum and intensity of the primary electron source. The simulation geometry also incorporated the major treatment-head components, including the target, flattening filter, primary collimator, secondary collimator jaws, and other components contributing to photon and neutron production. We used the resulting model to characterize the radiation field at the assumed therapist location and estimate the corresponding occupational dose. To evaluate the radiation field at the therapist's location, the photon fluence was calculated separately using the F5 tally in MCNP. We converted the energy-dependent fluence spectra from the simulation into equivalent dose rates using fluence-to-dose conversion coefficients. Because MCNP outputs are normalized per simulated particle or per machine workload unit, we normalized the results to the accelerator's actual clinical workload. In this study, the workload per patient was defined in terms of monitor units (MU), denoted as W_{patient}. Accordingly, the dose received by the therapist per patient, $H_{\text{staff, patient}}$, was calculated using the following relationship (NCRP, 2005):

$$H_{\text{staff, patient}} = W_{\text{patient}} \times t \times H \tag{2}$$

where t denotes the duration of the therapist's presence near the gantry head per patient, and H represents the dose per unit workload. Assuming a workload of N patients per day over D working days per year, the annual dose was determined using the following relationship (NCRP, 2005):

$$H_{\text{annual}} = H_{\text{staff, patient}} \times N \times D \tag{3}$$

3 Results

3.1 Validation

The validated results, as confirmed by Mesbahi et al.'s study (Mesbahi and Nejad, 2008), are shown in Fig. 3. This figure presents the validation of the Elekta accelerator before equipping it with an MLC. Also, the statistical uncertainty for calculating photon dose and fluence in this study was less than 1%, and for neutron dose and fluence, less than 5%. Because Mesbahi et al. validated their results against experimental data, we adopted the photon fluence spectrum from their study as the reference dataset. Accordingly, the percentage difference between the present results and those of Mesbahi et al. was calculated using the following equation:

$$\Delta(\%) = \frac{|F_{\text{this study}} - F_{\text{Mesbahi}}|}{F_{\text{Mesbahi}}} \tag{4}$$

In Eq. (4), F denotes the photon fluence at each point on the curve or within each energy interval. The discrepancy between the two curves was approximately 9% at the peak region, corresponding to an energy of about 0.4 MeV. This difference decreased to less than 5% over the 2-5 MeV energy range and became negligible toward the high-energy end of the spectrum. Overall, the mean discrepancy between the two studies was estimated to be below 5%.

Uncorrected Proof

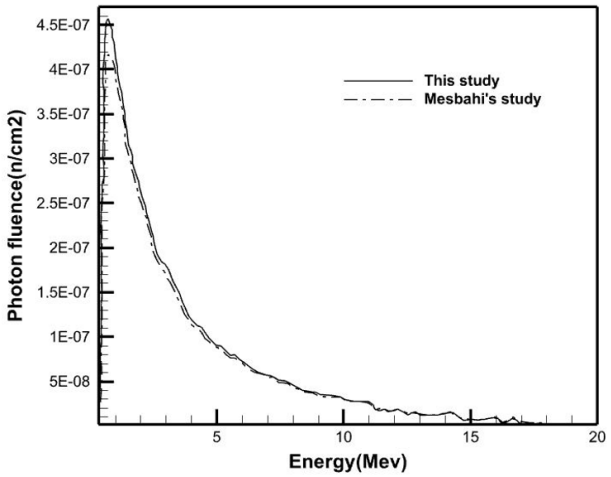


Figure 3: Photon spectrum on the phantom surface (per incident electron) at a distance of 100 cm from the accelerator source.

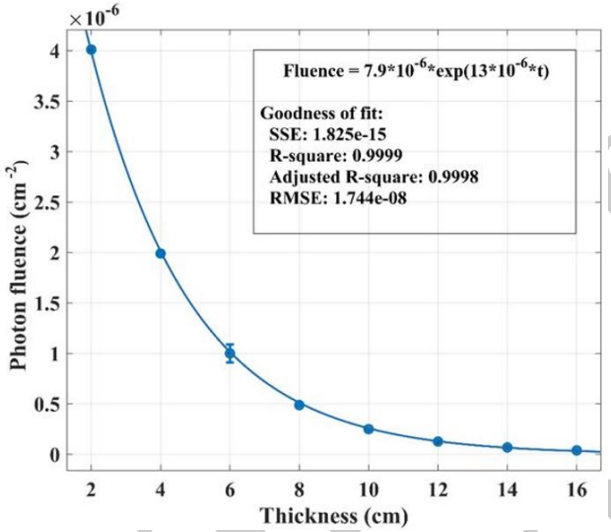


Figure 4: Calculation of photon fluence in air (per incident electron) behind varying thicknesses of Cerrobend shielding. The percentage of the standard deviation of the values ranges from 0.1% to 1%.

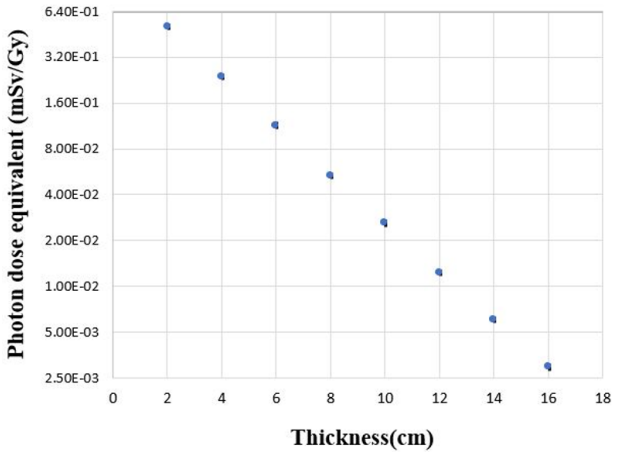


Figure 5: Calculation of the equivalent photon dose(mSv) per unit absorbed dose (Gy) behind the Cerrobend block in air for varying thicknesses ranging from 2 to 16 centimeters.

3.2 The effect of the Cerrobend block in reducing photon and neutron contamination

3.2.1 Photon fluence

Figure 4 illustrates that photon fluence decreases exponentially as the thickness of the Cerrobend block increases. This exponential decline is attributed to enhanced photon absorption and scattering within the shielding material. As thickness increases, the likelihood of photon interactions with Cerrobend's atomic constituents rises, significantly reducing the number of transmitted photons. This trend is consistent with the exponential attenuation law, which describes the decrease in radiation intensity as a function of absorber thickness. The high atomic numbers of Cerrobend's components-bismuth ($Z = 83$), tin ($Z = 50$), and lead ($Z = 82$)-contribute to its high photon attenuation efficiency, making it an effective shielding material. These results suggest that using a sufficiently thick Cerrobend block around the tumor can effectively minimize radiation exposure to surrounding healthy tissues.

3.2.2 Photon dose

The equivalent photon dose quantifies the energy absorbed per unit mass of tissue. It is calculated from the product of photon fluence, average photon energy, and the dose conversion coefficient. Consequently, photon dose is directly proportional to photon fluence. As shown in Fig. 5, photon dose decreases exponentially as shielding thickness increases. The detector, with a radius of 5 cm, was placed immediately behind the Cerrobend block to measure the remaining photon dose. The figure also shows that as thickness increases from 2 cm to 4 cm, the photon dose decreases by 63%. Meanwhile, as the thickness increases from 14 cm to 16 cm, the photon dose decreases by approximately 50%. Statistical analysis comparing the thicknesses of 2 cm- 16 cm demonstrated that all reductions were statistically significant.

3.2.3 Neutron fluence

Figure 6 illustrates the neutron fluence across different block thicknesses. The results demonstrate a general decline in neutron fluence as thickness increases from 2 cm to 14 cm. Beyond 14 cm, a marginal increase in fluence is observed; however, given the $\sim 5\%$ statistical error, this variation is not considered meaningful. The most pronounced reductions in neutron fluence occurred between 4-6 cm and 8-10 cm, whereas the smallest change was observed between 6-8 cm. For thicknesses ranging from 2 to 14 centimeters, differences in neutron fluence across the thicknesses are evident. For thicknesses between 14 to 16 centimeters, no clear difference in neutron fluence is observed. This suggests that variations in shield thickness from 14 to 16 centimeters do not have a meaningful impact on neutron fluence measurements.

Uncorrected Proof

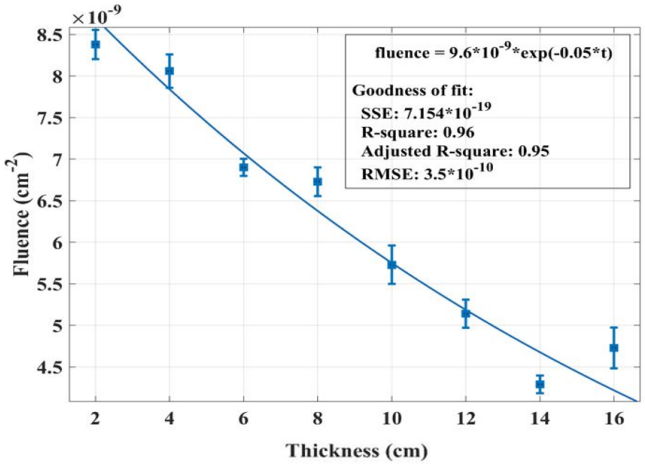


Figure 6: Calculation of neutron fluence in air (per incident electron) behind varying thicknesses of Cerrobend shielding. The percentage of the standard deviation of the values ranges from 1.5% to 5%.

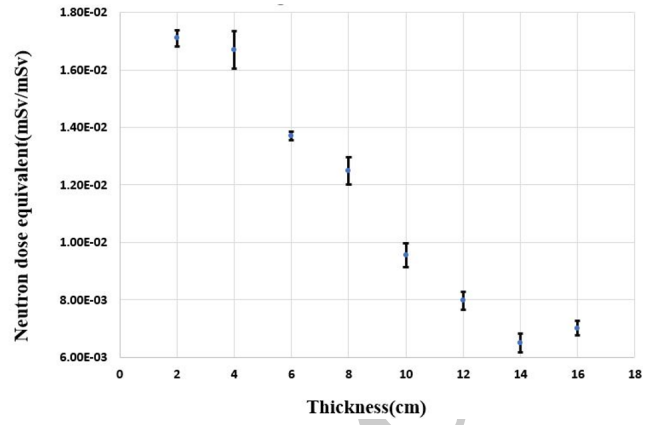


Figure 7: Calculation of the equivalent neutron dose (per millisievert of photon equivalent dose) behind the Cerrobend block in air for varying thicknesses ranging from 2 to 16 centimeters.

3.2.4 Neutron dose

Figure 7 shows that as thickness increases, the equivalent neutron dose decreases; However, this reduction is not significant. The largest reduction occurred at 10 cm, where the dose was 24% lower than at 8 cm. At a thickness of 16 cm, the neutron dose was approximately 9% higher than that at a thickness of 14 cm. In contrast, no significant difference in the equivalent neutron dose was observed between thicknesses of 14 cm and 16 cm.

3.3 The effect of BPE on reducing photon and neutron dose

To further reduce neutron dose, we incorporated BPE sheets of varying thicknesses into the Cerrobend block. The addition of 2 cm BPE reduced the photon dose by $\sim 4\%$ and the neutron dose by $\sim 20\%$. Increasing the BPE thickness to 4 cm linearly increased photon attenuation; however, beyond 4 cm, neutron attenuation efficiency declined. Figures 8-a and 8-b illustrate the impact of 4 wt% BPE on photon and neutron dose reduction, respectively. As shown in Fig. 8, the photon dose reduction followed an approximately linear trend across all thicknesses, whereas the neutron attenuation rate decreased for thicknesses > 4 cm. Table 2 summarizes the simulation results. Notably, neutron dose remained significant at all thicknesses except 16 cm. Because the photon dose reduction was consistent across all thicknesses, we omitted these results from the table for clarity. In general, an increase in the standard deviation is typically associated with reduced confidence in detected differences. This relationship stems from the fact that a larger standard deviation indicates greater dispersion or variability within the dataset. When data points are widely spread around the mean, the uncertainty in estimating true differences between group means rises.

3.4 Optimization of linear accelerator component configuration

Dose represents the dosimetric consequence of radiation transport and directly measures shielding effectiveness, whereas fluence characterizes particle transmission and attenuation under each accelerator configuration. Accordingly, the observed changes in photon and neutron fluence and dose can be attributed to modifications in the accelerator-head components and their configurations. The effect of MLC, FF, and wedge filter on the production of neutron and photon contamination was investigated. The result showed that when the FF is eliminated, there is no extreme variation in the dose rate (about 3%). Additionally, to examine the effect of the wedge on photoneutron production, we removed it, and it was found that upon removal of the wedge, the neutron fluence and dose increased by factors of 8 and 11, respectively.

Additionally, the photon fluence and dose increased by factors of 57 and 55, respectively. That is, the results showed that when the wedge is removed, the neutron dose increase-to-photon dose ratio is approximately 0.20, and neutron contamination is less. To examine the synergistic effect, we also removed the FF along with the wedge, and the results showed little difference from the case when the wedge alone was removed. For the case where only the MLC was removed, the photon and neutron doses increased by 23% and 120%, respectively. Additionally, by placing the MLC below the collimator (compared to the case where the MLC is positioned below the jaws), the photon dose and neutron dose decreased by 11% and 44%, respectively.

Shifting the MLC from beneath the jaws to beneath the PC reduces neutron contamination, and the changes in the magnitude were of statistical significance. The neutron contamination changes were of statistical significance in all the configurations, except the FFF mode (remove FF).

By replacing the material of the PC from tungsten to iron, the photon dose and fluence were unchanged. However, the neutron dose and fluence decreased by 10% and 7%, respectively. Table 3 summarizes the results. As shown in Table 3, removal of each accelerator-head component, except for the flattening filter, resulted in a re-

Under Peer Review

Table 2: Equivalent neutron and photon doses behind Cerrobend blocks of varying thicknesses, evaluated without and with the addition of the borated polyethylene plate.

Neutron dose in millisieverts per millisievert (mSv.mSv^{-1}) ± SD	Photon dose in millisievert per gray (mSv.Gy^{-1}) ± SD	Thickness (cm)	Measurement point	variable
$1.71 \times 10^{-2} \pm 2.70 \times 10^{-4}$	$5.10 \times 10^{-1} \pm 2.55 \times 10^{-3}$	2		
$1.67 \times 10^{-2} \pm 6.60 \times 10^{-4}$	$2.39 \times 10^{-1} \pm 1.19 \times 10^{-3}$	4		Position the
$1.37 \times 10^{-2} \pm 1.4 \times 10^{-4}$	$1.14 \times 10^{-1} \pm 9.12 \times 10^{-4}$	6	behind the	Cerrobend block at
$1.25 \times 10^{-2} \pm 4.75 \times 10^{-4}$	$5.30 \times 10^{-2} \pm 4.24 \times 10^{-4}$	8	Cerrobend	a distance of
$9.56 \times 10^{-3} \pm 4.21 \times 10^{-4}$	$2.60 \times 10^{-2} \pm 2.34 \times 10^{-4}$	10	block	70 cm
$7.97 \times 10^{-3} \pm 3.22 \times 10^{-4}$	$1.23 \times 10^{-2} \pm 1.60 \times 10^{-4}$	12	(in the air)	from the
$6.51 \times 10^{-3} \pm 3.25 \times 10^{-4}$	$6.00 \times 10^{-3} \pm 7.20 \times 10^{-5}$	14		source
$7.02 \times 10^{-3} \pm 2.43 \times 10^{-4}$	$2.94 \times 10^{-3} \pm 2.13 \times 10^{-5}$	16		
$5.27 \times 10^{-4} \pm 5.37 \times 10^{-6}$	$4.76 \times 10^{-3} \pm 3.61 \times 10^{-5}$	2	behind the	Placement of a
$4.31 \times 10^{-4} \pm 6.54 \times 10^{-6}$	$4.51 \times 10^{-3} \pm 2.82 \times 10^{-5}$	4	Cerrobend	BPE plate behind
$3.73 \times 10^{-4} \pm 8.03 \times 10^{-6}$	$4.34 \times 10^{-3} \pm 4.03 \times 10^{-5}$	6	block	the 8-cm-thick
$3.44 \times 10^{-4} \pm 6.33 \times 10^{-6}$	$4.16 \times 10^{-3} \pm 3.12 \times 10^{-5}$	8	(in water	Cerrobend
$3.20 \times 10^{-4} \pm 7.6 \times 10^{-6}$	$4.00 \times 10^{-3} \pm 2.73 \times 10^{-5}$	10	phantom)	block

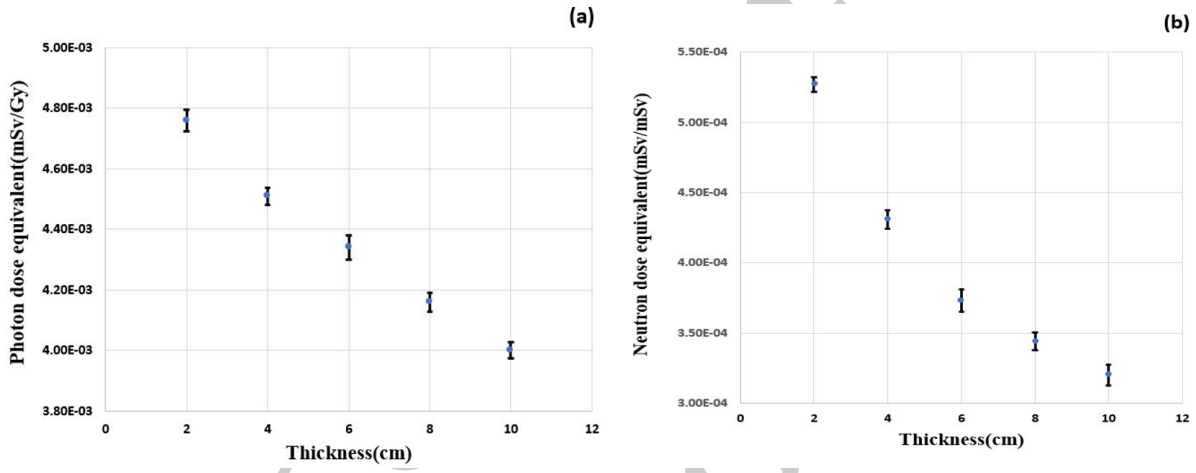


Figure 8: Incorporation of varying thicknesses of BPE into the 8 cm Cerrobend block and the subsequent calculation of (a) equivalent photon dose (mSv) per unit absorbed dose (Gy) behind the block within a water phantom; (b) neutron equivalent dose (per millisievert of photon equivalent dose) behind the block within a water phantom.

duction in the neutron equivalent dose. This finding may be attributed to photon and neutron attenuation as they traverse the accelerator head. Thicker components, particularly the wedge, absorb and scatter a larger fraction of the radiation; consequently, they have a greater effect on the outgoing photon and neutron fields. Because the wedge is thicker than the other components, at approximately 10 cm, it showed the greatest attenuation of both photons and neutrons.

In contrast, the flattening filter, less than 5 mm thick, did not produce a statistically significant reduction in neutron dose. The distance of each component from the target may also influence the photon and neutron doses. A substantial fraction of the photon and neutron fluence interacts first with the upper accelerator-head components located closer to the target. Consequently, a lower fluence reaches downstream components, such as the secondary collimator jaws, potentially reducing their contribution to radiation attenuation and photoneutron production (Chibani and Ma, 2003). In addition, component geometry may affect the observed dose variations. The FF typically has a thin, truncated-conical geometry.

In contrast, the jaws consist of opposing thick blocks of high-density material, commonly tungsten, that move to define the radiation field size. Material composition also matters: high-density, high-Z materials attenuate a greater fraction of photons, reducing the number of high-energy photons available to induce photonuclear reactions and produce photoneutrons. Because the neutron-emission threshold energy of iron is higher than that of tungsten, reaching approximately 11.2 MeV, photoneutron production in iron requires incident photons with energies of at least 11.2 MeV (NCRP, 1984). In contrast, tungsten exhibits a lower neutron-emission threshold of approximately 7.41 MeV (NCRP, 1984); consequently, under otherwise identical conditions, lower-energy photons can also induce photoneutron production in this material. Therefore, the likelihood of photoneutron reactions is expected to be higher in tungsten than in iron. Figure 9 illustrates the photon fluence and the photoneutron fluence generated in the iron and tungsten collimators. As shown, the neutron fluence produced in the iron collimator is slightly lower than that generated in the tungsten collimator.

Uncorrected Proof

Table 3: Changes in photon and neutron dose and fluence in different configurations of FF, Wedge Filter, MLC, Jaws and PC.

Changes in neutron dose	Changes in photon dose	Changes in neutron fluence	Changes in photon fluence	Type of configuration
3% decrease	3% increase	2% decrease	3% increase	Remove FF
Increase by a factor of 11	Increase by a factor of 55	Increase by a factor of 8	Increase by a factor of 57	Remove wedge
Increase by a factor of 2.2	23% increase	Increase by a factor of 1.3	36% increase	Remove MLC
80% increase	10% increase	84% increase	12% increase	Different configuration (transferring the MLC from beneath the PC to beneath the jaws)
10% decrease	Insignificant	7% decrease	Insignificant	Changing the material of the PC from tungsten to iron

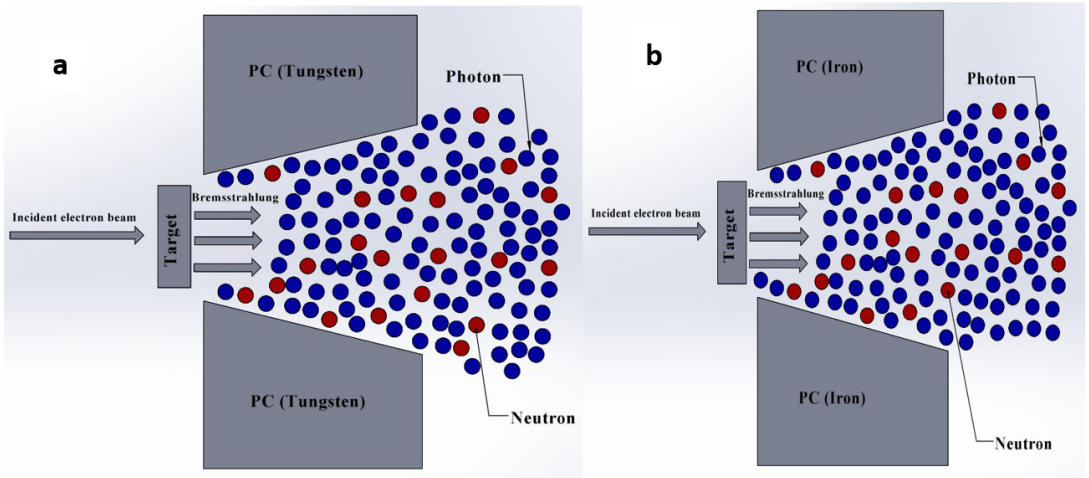


Figure 9: Neutron production from the primary collimator: (a) tungsten collimator; (b) iron collimator.

3.5 Estimation of annual occupational dose

The maximum annual dose a treatment therapist receives from induced radioactivity can be estimated based on the treatment machine's observed operating pattern. Assuming a 15-minute treatment time, with the therapist remaining in the treatment room for 5 minutes per patient and standing adjacent to the treatment head, the mean dose rate-calculated from an average time beginning 2 minutes after irradiation-was estimated at 0.29 μSv.h^{-1} per patient. Under these assumptions, the corresponding annual dose would be approximately 2.6 mSv for a therapist working full-time with the machine for 48 weeks per year. However, this value represents a conservative maximum estimate, since the induced dose rate decreases substantially during the 5-minute interval in which the therapist is assumed to remain in the treatment room.

4 Discussion

Taherkhani et al. measured the attenuation coefficient of Cerrobend blocks for 6 and 15 MV photon beams generated by an Elekta linear accelerator using Kodak Extended Dose Range (Kodak, USA) films (MS et al., 2010). By incrementally increasing the block thickness from 1 cm to 10 cm in 1 cm steps, they observed that radiation intensity decreases exponentially at both energy levels. However, the attenuation slope in their study was slightly steeper than that observed in the present study. This discrepancy may be attributed to the strong dependence of the attenuation coefficient on beam energy and beam-hardening effects. Since the beam energy in their study was lower, the higher measured attenuation coefficient is justifiable.

Mohammadi et al. examined the Influence of various Cerrobend block parameters on dose reduction (Mohammadi et al., 2014a). They evaluated relative dose distribution using Kodak EDR2 films placed between RW3 water-equivalent slabs. Their findings showed that increasing block width substantially reduced dose in the protected area at all measured depths. Specifically, broadening the block limited scattered radiation reaching the shielded region and reduced the central axis dose. They reported that, for large fields, increasing the block width by 1 cm resulted in an approximate 10% reduction in dose within the protected area, indicating that narrow Cerrobend blocks are inadequate for complete shielding. They also found that increasing block height significantly reduced dose in the protected zone, with maximum dose reduction at a depth of 5 cm-consistent with our study. They also noted that increasing block height from 70-80 mm to 90-95 mm

Uncorrected Proof

led to a marked dose decrease. In contrast, Khan et al. suggested that a block thickness of 7-8 cm is sufficient to protect healthy tissue (Khan and Gibbons, 2014).

Tellili et al. computed the total mass attenuation coefficient (m), half-value layer (HVL), and tenth-value layer (TVL) for six Cerrobend alloys across a photon energy range of 0.1 MeV to 100 GeV (Tellili et al., 2017). Their results showed that these shielding parameters vary with both incident photon energy and the alloy's chemical composition. At low photon energies, where photoelectric absorption dominates, this dependence is most pronounced. As photon energy increases to intermediate levels, Compton scattering becomes the prevailing interaction, reducing the Influence of composition and energy on attenuation parameters. At high energies, pair production dominates, rendering attenuation values nearly energy-independent but again sensitive to composition. Among the alloys examined, shielding effectiveness ranked from highest to lowest as: Safe alloy, Bend alloy, Low 147 alloy, Low 136 alloy, Tru alloy, and Cast alloy. Their findings confirms that the Bend alloy used in our study is a relatively effective shielding material against gamma radiation.

Bahreyni Tousi et al. used the MCNPX Monte Carlo simulation code to model a Cerrobend block measuring $1.5 \times 1.5 \times 7$ cm^3 (Toossi et al., 2018). Simulations were conducted in a 10×10 cm^2 radiation field at a 100 cm source-to-surface distance, measuring neutron doses at depths of 0.5, 2, and 3 cm in a water phantom. Neutron dose calculations used the F4 tally with fluence-to-dose conversion factors and the F6 tally. Without the block, neutron doses were 0.57, 0.55, and 0.54 mSv.mSv^{-1} at the respective depths. With the Cerrobend block in place, neutron doses decreased by 12%, 13%, and 17%. In comparison, our study demonstrated an approximately 10% greater reduction in neutron dose using a 6 cm thick block. These differences may stem from methodological variations: Bahreyni Tousi et al. used F4 tallies in a water phantom, while our work used the F5 tally with air-based fluence-to-dose factors. In a follow-up study, they used CR-39 nuclear track detectors and concluded that Cerrobend blocks contributed significantly to neutron contamination, second only to the wedge (Khajetash et al., 2019). However, the apparent absence of neutron dose at a 4 cm depth in their open-field setup likely reflects the limited sensitivity of CR-39 detectors. Studies using Bonner spheres and Optically Stimulated Luminescence (OSL) techniques have shown strong agreement with Monte Carlo simulations, supporting the reliability of the MCNP model (Mohammadi et al., 2015; Israngkul-Na-Ayuthaya et al., 2015).

Physically, the observed reduction in neutron fluence with increasing Cerrobend thickness can be attributed to photon interaction within the shielding material, which leads to photon attenuation and scattering. As photon fluence decreases, photoneutron production diminishes accordingly. This relationship also affects the dose rate: lower photon fluence leads to a reduced dose rate, fewer monitor units (MUs), and consequently a lower neutron dose.

Several studies have highlighted BPE as an effective neutron shielding material. For example, Wang et al. demonstrated that it significantly reduces both neutron fluence and photon levels at the maze wall corner (Wang et al., 2011). This dual attenuation arises from the material's capacity to scatter and absorb photons, reducing photon fluence and the likelihood of photoneutron production. Lower dose rates and fewer MUs subsequently reduce neutron doses. Additionally, BPE absorbs photoneutrons produced by accelerator components, generating secondary gamma rays that Cerrobend blocks and then filters.

Khabaz analyzed the effects of removing individual components of an 18 MV Varian linear accelerator on the average photon and neutron energies along the central axis using MCNPX (Khabaz, 2018). Contrary to earlier studies, his findings showed that removing any accelerator component did not significantly affect neutron fluence (Naseri and Mesbahi, 2010; Mohammadi et al., 2015). Photon fluence at the isocenter increased following component removal, with the greatest increase occurring after eliminating the FF-a result inconsistent with our findings. This discrepancy may stem from the FF's minimal central thickness, which has limited Influence on central-axis photon fluence. Its effects are more prominent at the field periphery, especially with large field sizes (Bencheikh et al., 2017). Several studies also suggest that the FF contributes less to photoneutron production than other components (Pena et al., 2005; Dowlatabadi et al., 2020). Pena et al., for instance, reported that MLC contribution to neutron production was only 6% in a Siemens PRIMUS accelerator at 15 MV (Pena et al., 2005).

In contrast, our results demonstrate that neutron fluence and dose are significantly influenced by changes in MLC configuration. This inconsistency may be due to Pena et al.'s use of the F1 tally, which does not provide energy information on emitted neutrons. Since our study focuses on neutron dose impacts on patients, the F5 tally is a more appropriate choice.

Furthermore, our study found a direct correlation between photon and neutron fluence after removing specific accelerator components. For example, removing the FF or altering the PC material led to minor changes in both photon dose and neutron production. These findings align with Dowlatabadi et al., who reported that changes in photon and electron energy spectra directly influence neutron generation (Dowlatabadi et al., 2020).

For personnel working in controlled areas, where their duties may involve a substantial likelihood of exposure to ionizing radiation, some publications (NCRP, 1993) have recommended an annual effective-dose limit of 50 mSv.y^{-1}. They also state that the cumulative effective dose should not exceed 10 mSv multiplied by the worker's age in years. Accordingly, the shielding design objective for new facilities should be set below this cumulative-dose criterion rather than at the regulatory limit itself. According to the ICRP recommendations (Protection, 2007), the occupational effective-dose limit is 20 mSv per year averaged over five years, corresponding to 100 mSv in five years, with no single year exceeding 50 mSv. Because the result of the present study appears to be substan-

Uncorrected Proof

tially lower than the dose limits reported by the ICRP, the scope of this estimate should be clearly defined. The reported estimate considers only the technician's exposure under the assumed scenario of presence inside the treatment room, adjacent to the treatment head. It does not separately account for the dose received while the technician is stationed at the console or in the control room. This study aimed to optimize the accelerator components and shielding system for evaluating the dose received by a water phantom rather than a patient. Accordingly, the treatment-room and bunker geometry was intentionally excluded from the present model because the primary goal was to optimize the accelerator components and shielding configuration under controlled, simplified conditions rather than to reproduce the complete clinical treatment environment. This approach allowed us to evaluate the dose contributions from the accelerator head and the local shielding assembly independently, without introducing additional effects from room geometry, structural materials, or treatment-room barriers. Our estimated maximum annual dose (2.6 mSv) closely agreed with the findings of Rawlinson et al., who determined an annual dose of 2.9 mSv under similar 18 MV operating conditions for a Varian 21EX (Rawlinson et al., 2002).

Component thickness is the primary determinant of variations in photoneutron fluence following component removal. For instance, wedges-being thicker than most components-yield the most pronounced reductions in neutron fluence upon removal. Conversely, the FF, due to its limited thickness, exhibits minimal Influence. Additionally, when the MLC is placed beneath the PC, it absorbs and scatters photons, limiting their interaction with downstream components such as jaws and wedges, thereby reducing neutron fluence. However, when the MLC is situated below the jaws, it encounters photons that have already passed through, leading to higher neutron fluence. In this scenario, increasing field size has minimal effect: while jaw-generated neutron production decreases with field size, MLC-generated neutron production increases. Our findings also show that using iron in the PC results in lower neutron fluence than tungsten, a difference attributable to iron's higher neutron emission threshold energy.

5 Conclusions

This study showed that the greatest reduction in neutron dose for Cerrobend shielding was achieved by increasing its thickness from 8 to 10 cm, resulting in a 23% decrease. Similarly, increasing the thickness of borated polyethylene from 2 to 4 cm reduced the neutron dose by 18%. However, further increases in borated polyethylene thickness did not produce an appreciable additional reduction in neutron dose. Therefore, among the evaluated configurations, a combination of 10-cm-thick Cerrobend and 4-cm-thick borated polyethylene is the most effective shielding arrangement.

The ambient neutron dose was normalized to the delivered photon dose (expressed in $Sv.h^{-1}$) for each accelerator configuration. With respect to accelerator-head components, removal of the FF reduced the neutron dose from 91 to 88.27 $\mu Sv.h^{-1}$. Considering the approximately 3% statistical uncertainty, this reduction was not statistically significant. In contrast, removal of the wedge increased the neutron dose to 997 $\mu Sv.h^{-1}$. Removing the MLC increased the neutron dose to 200.2 $\mu Sv.h^{-1}$, whereas relocating the MLC from beneath the PC to beneath the jaws resulted in 163 $\mu Sv.h^{-1}$. Furthermore, replacing the tungsten PC with an iron collimator reduced the neutron dose to 82.12 $\mu Sv.h^{-1}$. Accordingly, among the configurations evaluated, the optimal accelerator-head design for minimizing neutron dose retains all components, places the MLC beneath the PC, positions the wedge above the jaws, and uses iron rather than tungsten for the PC.

Acknowledgements

We thank all colleagues and institutions that supported this study.

Conflict of Interest

The authors declare no potential conflict of interest regarding the publication of this work.

Funding

The authors declare that no funds, grants, or other financial support were received during the preparation of this manuscript.

References

Banaee, N., Goodarzi, K., and Nedaie, H. A. (2021). Neutron contamination in radiotherapy processes: a review study. *Journal of Radiation Research*, 62(6):947–954.

Becker, J. (2007). Simulation of neutron production at a medical linear accelerator. *Institute of Experimental Physics University of Hamburg, MSc Diploma Thesis*, pages 28–30.

Bencheikh, M., MAGHNOUJ, A., and TAJMOUATI, J. (2017). Study of Flattening Filter Effects on the Off-Axis Ratio and the Dose Delivered by 6 MV Photon Beam Produced by Varian Clinac 2100 in a Water Phantom. *Applied Journal of Environmental Engineering Science*, 3(1):J–Envir.

Cheraghian, M., Pourfallah, T., Sabouri-Dodaran, A. A., et al. (2021). Calculation of photoneutron contamination of varian linac in icru soft-tissue phantom using MCNPX code. *Journal of Medical Physics*, 46(2):116.

Chibani, O. and Ma, C.-M. C. (2003). Photonuclear dose calculations for high-energy photon beams from Siemens and Varian linacs. *Medical Physics*, 30(8):1990–2000.

Dowlatabadi, H., Mowlavi, A., Ghorbani, M., et al. (2020). Study of photoneutron production for the 18 mv photon beam of the siemens medical linac by Monte Carlo simulation. *Journal of Biomedical Physics & Engineering*, 10(6):679.

Facure, A., Falcao, R., Silva, A. d., et al. (2005). A study of neutron spectra from medical linear accelerators. *Applied Radiation and Isotopes*, 62(1):69–72.

Uncorrected Proof

Hendricks, J. S., McKinney, G. W., Waters, L. S., et al. (2005). MCNPX Extensions Version 2.5. 0. *Los Alamos National Laboratory*, 15.

Israngkul-Na-Ayuthaya, I., Suriyapee, S., and Pengvanich, P. (2015). Evaluation of equivalent dose from neutrons and activation products from a 15-MV X-ray LINAC. *journal of Radiation Research*, 56(6):919–926.

Johns, H. E., Cunningham, J. R., et al. (1983). The physics of radiology.

Khabaz, R. (2018). Effect of each component of a LINAC therapy head on neutron and photon spectra. *Applied Radiation and Isotopes*, 139:40–45.

Khajetash, B., Toossi, M. T. B., Ghorbani, M., et al. (2019). Measurement of fast neutron contamination caused by the presence of wedge and block using CR-39 detector. *Journal of Cancer Research and Therapeutics*, 15(Suppl 1):S103–S109.

Khan, F. M. and Gibbons, J. P. (2014). *Khan's the physics of radiation therapy*. Lippincott Williams & Wilkins.

Koch, H. W. and Motz, J. (1959). Bremsstrahlung cross-section formulas and related data. *Reviews of Modern Physics*, 31(4):920.

Kumar, A., Kaur, R., Dong, M., et al. (2018). Radiation interaction parameters of dosimetric importance for some commonly used compensators in IMRT using Monte Carlo simulation code. *Journal of Radiological Protection*, 38(4):1321–1343.

Ma, A., Awotwi-Pratt, J., Alghamdi, A., et al. (2008). Monte carlo study of photoneutron production in the Varian Clinac 2100C linac. *Journal of Radioanalytical and Nuclear Chemistry*, 276(1):119–123.

Mao, X., Kase, K., Liu, J., et al. (1997). Neutron sources in the varian clinac 21000/23000 medical accelerator calculated by the EGS4 code. *Health Physics*, 72(4):524–529.

Martinez-Ovalle, S., Barquero, R., Gomez-Ros, J., et al. (2011). Neutron dose equivalent and neutron spectra in tissue for clinical linacs operating at 15, 18 and 20 MV. *Radiation Protection Dosimetry*, 147(4):498–511.

Mendes, R. M., Silva, M. G., Rebello, W. F., et al. (2022). Influence of radiotherapy room shielding on ambient dose equivalent due to photons H*(10) p and neutrons H*(10) n in the patient's plane. *Applied Radiation and Isotopes*, 181:110095.

Mesbahi, A. and Nejad, F. S. (2008). Monte Carlo study on a flattening filter-free 18-MV photon beam of a medical linear accelerator. *Radiation Medicine*, 26(6):331–336.

Mohammadi, M., Taherkhani, A., and Saboori, M. (2014a). Radiation dose distribution under the area protected using a cerrobend block during external beam radiotherapy: a film study. *Journal of Radiotherapy in Practice*, 13(4):456–464.

Mohammadi, N., Miri-Hakimabad, H., Rafat-Motavlli, L., et al. (2015). Neutron spectrometry and determination of neutron contamination around the 15 MV Siemens Primus LINAC. *Journal of Radioanalytical and Nuclear Chemistry*, 304(3):1001–1008.

Mohammadi, N., Miri-Hakimabad, S., and Rafat-Motavalli, L. (2014b). A Monte Carlo study for photoneutron dose estimations around the high-energy linacs. *Journal of Biomedical Physics & Engineering*, 4(4):127.

MS, S. et al. (2010). Evaluation of the physical characteristic of cerrobend blocks used for radiation therapy.

Naseri, A. and Mesbahi, A. (2010). A review on photoneutrons characteristics in radiation therapy with high-energy photon beams. *Reports of Practical Oncology and Radiotherapy*, 15(5):138–144.

NCRP (1984). *Neutron Contamination from Medical Electron Accelerators: Recommendations of the National Council on Radiation Protection and Measurements*. Number 79. Ncrp.

NCRP (1993). National Council on Radiation Protection and Measurements. Limitation of exposure to ionizing radiation. Bethesda (MD. NCRP Report No.: 116.

NCRP (2005). National Council on Radiation Protection and Measurements. Structural shielding design and evaluation for megavoltage X- and gamma-ray radiotherapy facilities. Bethesda (MD). NCRP Report No.: 151.

Ng, J., Gregucci, F., Pennell, R. T., et al. (2023). MRI-LINAC: A transformative technology in radiation oncology. *Frontiers in Oncology*, 13:1117874.

Paredes, L., Balcazar, M., Genis, R., et al. (2001). Leakage neutron radiation in a medical electron accelerator. In *AIP Conference Proceedings*, volume 593, pages 140–147. American Institute of Physics.

Pena, J., Franco, L., Gomez, F., et al. (2005). Monte Carlo study of Siemens PRIMUS photoneutron production. *Physics in Medicine & Biology*, 50(24):5921–5933.

Piotrowski, T. (2020). Shielding concrete with neutron attenuating and absorbing components. In *Micro and Nanostructured Composite Materials for Neutron Shielding Applications*, pages 177–218. Elsevier.

Protection, R. (2007). ICRP publication 103. *Ann Icrp*, 37(2.4):2.

Rajesh, K., Ganapathi, R. R., Musthafa, M., et al. (2020). A passive method for absolute dose evaluation of photoneutrons in radiotherapy.

Rawlinson, J. A., Islam, M. K., and Galbraith, D. M. (2002). Dose to radiation therapists from activation at high-energy accelerators used for conventional and intensity-modulated radiation therapy. *Medical Physics*, 29(4):598–608.

Sahin, M. C., Manisa, K., Bircan, H., et al. (2024). Experimental, theoretical, and biological investigations on radiation shielding parameters of boron-doped cerrobend alloys. *Matéria (Rio de Janeiro)*, 29(4):e20240366.

Seif, F., Tahmasebi-Birgani, M., and Bayatiani, M. (2017). An analytical-empirical calculation of linear attenuation coefficient of megavoltage photon beams. *Journal of Biomedical Physics & Engineering*, 7(3):225.

Tellili, B., Elmahroug, Y., and Souga, C. (2017). Investigation on radiation shielding parameters of cerrobend alloys. *Nuclear Engineering and Technology*, 49(8):1758–1771.

Uncorrected Proof

Toossi, M. B., Khajetash, B., and Ghorbani, M. (2018). Assessment of neutron contamination originating from the presence of wedge and block in photon beam radiotherapy. *Journal of Biomedical Physics & Engineering*, 8(1):3.

Wang, X., Esquivel, C., Nes, E., et al. (2011). The neutron dose equivalent evaluation and shielding at the maze entrance of a Varian Clinac 23EX treatment room. *Medical Physics*, 38(3):1141–1149.

Zanini, A., Durisi, E., Fasolo, F., et al. (2004). Monte carlo simulation of the photoneutron field in linac radiotherapy treatments with different collimation systems. *Physics in Medicine & Biology*, 49(4):571–582.

©2027 by the journal.

RPE is licensed under a Creative Commons Attribution-NonCommercial 4.0 International License (CC BY-NC 4.0).

To cite this article:

M.H. Jahanimehr and S.M.M. Abtahi. Mitigation of photoneutron contamination in high-energy LINACs via component reconfiguration and advanced shielding *Radiation Physics and Engineering*, In Press.

DOI:

To link to this article:

Uncorrected Proof